Acta Materialia 294 (2025) 121158

Contents lists available at ScienceDirect

Acta Materialia

journal homepage: www.elsevier.com/locate/actamat

Full length article

Superstoichiometric (Al,Cr)N: Nitrogen's whereabouts and role in structure-property relationships

F.F. Klimashin [a,*], M. Učík [b,c], M. Matas [d], D. Holec [d], M. Beutner [e], M. Hackert-Oschätzchen [e], A. Xomalis [a,f], J.J. Schwiedrzik [a,g], J. Klusoň [b], M. Jílek [b], A. Lümkemann [h], J. Michler [a,i], T.E.J. Edwards [a,j]

[a] Empa – Swiss Federal Laboratories for Materials Science and Technology, Laboratory for Mechanics of Materials and Nanostructures, Feuerwerkerstrasse 39, Thun 3602, Switzerland
[b] PLATIT a.s., Průmyslová 3020, Šumperk 787 01, Czech Republic
[c] Masaryk University, Faculty of Science, Kotlářská 2, Brno 611 37, Czech Republic
[d] Montanuniversität Leoben, Department of Materials Science, Franz-Josef-Strasse 18, Leoben 8700, Austria
[e] Otto von Guericke University Magdeburg, Chair of Manufacturing Technology with Focus Machining, Universitätsplatz 2, Magdeburg 39106, Germany
[f] Norwegian University of Science and Technology, Department of Electronic Systems, Nanoelectronics and Photonics Group, Trondheim 7034, Norway
[g] Empa – Swiss Federal Laboratories for Materials Science and Technology, Laboratory for High Performance Ceramics, Ueberlandstrasse 129, Duebendorf 8600, Switzerland
[h] PLATIT AG, Eichholzstrasse 9, Selzach 2545, Switzerland
[i] EPFL, Institute of Materials, Lausanne 1015, Switzerland
[j] National Institute for Materials Science, Research Center for Structural Materials, 1-2-1 Sengen, Tsukuba, Ibaraki 305-0047, Japan

ARTICLE INFO

Keywords:
(Al,Cr)N
Superstoichiometry
Point defects
Microstructure
Hardness
Fracture toughness
Wear resistance

ABSTRACT

The role of light elements in ceramic materials cannot be overestimated. By tuning their concentration, a whole multitude of mechanisms can be activated, directly influencing the material's functional properties. However, accurate determination of light element concentrations remains a challenge and is often, especially in superstoichiometric compounds, overlooked. Here, we provide atomic-scale insight into nitrogen incorporation in superstoichiometric (Al,Cr)N_x coatings ($x = 1.01–1.11$) with similar Al/(Al+Cr) ratios (0.59–0.63) by combining elemental concentrations, stress-free lattice parameters, and *ab initio* calculations. Below a threshold of $x \approx 1.06–1.08$, excess nitrogen predominantly occupies interstitial lattice sites, while beyond this point, it can also incorporate into vacant metal sites (anti-sites).

We then conducted a detailed investigation on two superstoichiometric coatings: (Al,Cr)$N_{1.08}$, with nitrogen near the threshold, and (Al,Cr)$N_{1.11}$, which exceeds it. While (Al,Cr)$N_{1.08}$ features densely packed, elongated fibrous grains with a strong (111) growth orientation, (Al,Cr)$N_{1.11}$ develops a fine-grained microstructure with a (220) growth orientation. These structural changes significantly affect mechanical properties: (Al,Cr)$N_{1.08}$ is 9 % harder (34.4 GPa vs. 31.6 GPa) with superior abrasive resistance, while (Al,Cr)$N_{1.11}$ has 9 % higher fracture toughness (4.15 MPa$\sqrt{m}$ vs. 3.80 MPa$\sqrt{m}$) and enhanced microcracking and crack-branching behaviour. Our findings not only demonstrate the tunability of mechanical properties in superstoichiometric (Al,Cr)N_x coatings but also highlight the broader potential of superstoichiometric nitrides and ceramics for advanced applications.

1. Introduction

Ceramic materials including metal carbides, nitrides, and oxides, are widely used in modern applications due to their exceptional properties, such as high melting points, mechanical strength, and chemical stability. Many of these materials are strongly non-stoichiometric compounds, characterised by broad homogeneity ranges in their phase diagrams [1].

Deviations from stoichiometry can occur in various ways leading to the formation of both substoichiometric and superstoichiometric compounds. The substoichiometric compounds often form due to anion vacancies, which are thermodynamically inevitable in crystalline solids as they increase entropy. Their concentration in metal carbides, nitrides,

* Corresponding author.
E-mail address: fedor.klimashin@empa.ch (F.F. Klimashin).

https://doi.org/10.1016/j.actamat.2025.121158
Received 14 February 2025; Received in revised form 13 April 2025; Accepted 19 May 2025
Available online 19 May 2025

and oxides can exceed 50 % without destabilising the crystal structure. Non-equilibrium synthesis techniques, such as physical vapour deposition (e.g., magnetron sputtering), can produce even higher concentrations of anion vacancies [2], further expanding the homogeneity range of these materials. In contrast, superstoichiometry can arise from multiple types of point defects. While in some superstoichiometric compounds, such as cubic $(Ti_{0.5}Al_{0.5})N$, cation vacancies are energetically favoured over other point defects [3], in others, like CrN, nitrogen atoms occupying interstitial or anti-site positions are as likely as cation vacancies [4].

The role of point defects in such materials cannot be overestimated. By tuning their concentration, a whole multitude of mechanisms can be activated that directly influence the properties. The effects of vacancies, particularly in substoichiometric compounds, have been extensively studied. They can, for instance, affect valence electron concentration and with that the occupancy of shear-sensitive and shear-resistant bonding states, thus directly influencing hardness [5], elastic properties [6] and fracture toughness [7–9]. Vacancies can also exert strains on the surrounding crystal lattice, with the lattice strain fields impeding the motion of dislocations and as such resulting in strengthening and hardening [1,10,11]. They can also improve the electrocatalytic performance [12], optical properties [13,14], and significantly affect the formation energy allowing to stabilise metastable materials [15–17].

However, the impact of other point defects, such as interstitials, on structure-property relationships remains largely unexplored. This lack of knowledge inspired our investigation into superstoichiometric (Al,Cr)N_x coatings ($x > 1$). We recently produced a series of (Al,Cr)N_x coatings with x ranging from 1.01 to 1.08 via reactive sputtering of a compound target at high power densities using a DC power supply [18]. (These power densities are comparable to the peak power densities in high-power impulse magnetron sputtering, HiPIMS [19–21], yet since the sputtering process is continuous and not pulsed, it is more accurately referred to as high-ionisation magnetron sputtering, HIMS [22].) However, the localisation of excess nitrogen and the superstoichiometry effects have not been addressed [18]. Here, we extended the x range to 1.11 and, by combining computational and experimental techniques, identified the locations of excess nitrogen in superstoichiometric (Al,Cr)N_x coatings, providing fundamental explanations for their properties and cutting performance. These findings are envisioned to be applicable to other superstoichiometric ceramic coatings, particularly metal nitrides.

2. Materials and methods

2.1. Experimental

The coatings were deposited in a π411 industrial PVD unit (PLATIT a.s., Czech Republic) from an $Al_{60}Cr_{40}$ tubular target (99.95 % purity, Ø110 × 510 mm, PLANSEE Composite Materials GmbH, Germany) using a DC power supply with a total output power of 25 kW (peak power densities of 840 W/cm^2). The (Al,Cr)N_x coatings with x values ranging from 1.01 to 1.08 were produced in our previous study by varying nitrogen pressure, bias voltage, and magnetic field strength (see Ref. [18]). Two additional coatings were deposited here: one within the established range ($x = 1.06$) for verification purposes, and one outside this range ($x = 1.11$) to explore superstoichiometry across a broader x range. (Table S1 in the Supplementary Material provides an overview of the elemental compositions of coatings included in both the present work and our previous study.) Of particular interest were two coatings with $x = 1.08$ and 1.11, which underwent detailed microstructural and micromechanical analyses, as well as cutting tests. All coatings were deposited on WC—Co (SANDVIK Grade H10F, 10 mol. % Co) substrates at 480 °C. For TEM and micromechanical studies, coatings with thickness of about 10 μm were deposited on Co-free WC substrates (PLANSEE Composite Materials GmbH, Germany).

Bragg-Brentano X-ray diffraction (BBXRD) of monochromised CuK_α radiation ($\lambda = 1.5406$ Å) was used to gain information about the constituent phases and preferential orientation, while glancing-angle XRD (GAXRD) with an incident angle γ of 3° was used to assess the stress-free lattice parameter and residual stresses of the cubic phase based on a modified $\sin^2\psi$ method [23].

Chemical composition was determined by energy dispersive X-ray spectroscopy (EDS), which was calibrated using a CrN standard (Ardennes Analytique Hungary Kft). To confirm the changes in the nitrogen concentration, we furthermore performed elastic recoil detection analysis (ERDA) using a 13-MeV ^{127}I ion beam and combining a time-of-flight spectrometer with a gas ionisation chamber [24], and Raman spectroscopy (HeNe laser, 632.8 nm). A detailed transmission electron microscopy (TEM, FEI Titan Themis 200, ThermoFisher) study of focused ion beam (FIB) prepared liftouts used bright- and dark-field TEM as well as high-resolution (HR-TEM) imaging. The selected area electron diffraction (SAED) isolates a 4-μm diameter region of the sample.

Nanoindentation analysis was carried out using a quasi-continuous stiffness measurement (QCSM) technique (ZwickRoell). For a detailed description of the technique as well as the tip area function and instrument compliance calibration see Refs. [18,25]. A test on bulk reference Al_2O_3 yields indentation hardness, H, of 24.9 ± 2.0 GPa and modulus, E, of 413 ± 16 GPa, thus providing a lower bound of the previously reported values [25–27]. Using a Berkovich diamond tip under the maximum load of 200 mN and analysing the load–displacement curves according to Oliver and Pharr [27], depth-resolved H and E profiles of the coatings were obtained. The evaluation of the coating-only H and E is described in detail by Fischer-Cripps [28]. A Poisson's ratio of stoichiometric fcc-(Al,Cr)N shows only minor departures from 0.2 for the Al/(Al+Cr) ratios within the range 0.59–0.63 as follows from the *ab initio* calculations [29].

Fracture toughness was assessed using the micropillar splitting technique [30]. The micropillars were fabricated using a Ga^+ FIB (Lyra3, Tescan, Czech Republic) in a two-step process. The rough milling to 5 μm diameter was performed at about 4 nA, while polishing down to about 3 μm was done at about 200 pA. In-SEM micropillar splitting tests were carried out using a nanoindenter (Alemnis AG, Switzerland) in displacement-controlled mode using a cube-corner tip (Synton AG, Switzerland). The critical load for fracture, P_C, along with the pillar radius, R, was used to evaluate the fracture toughness, K_C:

$$K_c = \gamma \frac{P_c}{R^{3/2}} \quad (1)$$

with γ being a coefficient depending on the indenter tip geometry as well as hardness and Young's modulus of the coating [31].

To evaluate the cutting performance of the coatings in real working conditions, two types of cutting tests were conducted: face milling and fly cutting (a single-tooth cutting test simulating gear hobbing [32]). The face milling tests with minimum quantity lubrication (MQL) were performed on Fehlmann Picomax 60-M (Fehlmann AG, Switzerland). The selected coatings were deposited on end mills (MB-NVDS, Fraisa AG, Switzerland) which were then used to machine a C45 steel plate (HB 200) with the following composition: 0.45 wt. % C, 0.67 wt. % Mn, 0.27 wt. % Si, 0.21 wt. % Cr, 0.13 wt. % Ni, 0.10 wt. % Cu, 0.006 wt. % P, 0.001 wt. % S. The cutting speed and feed rate were set to 200 m/min and 0.32 mm/rev, respectively, with radial and axial cutting depths of 4 mm each. Total tool wear was assessed after removing 2500 cm^3 of material from the steel plate. The dry fly cutting of 20MnCr5 (AISI5120H, HRB 85) gear blanks was carried out on a Liebherr LC180 gear cutting machine using the teeth (PM-HSS type S390) from an original hob obtained by wire erosion [33]. The gearing parameters were set to a modulus of 4 mm, a pressure angle of 20°, gear width of 60 mm and a tip diameter of 114 mm. Cutting speed and feed rate were set to 220 m/min and 6.9 mm/rev, respectively. The wear resistance was evaluated once the flank wear exceeded 130 μm or the crater wear exceeded 100 μm.

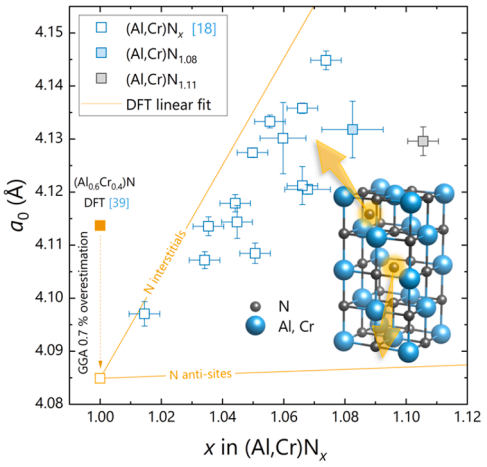

Fig. 1. Stress-free lattice parameter, a_0, of (Al,Cr)N$_x$ as a function of nitrogen content, x, determined experimentally and computationally (weighted average of CrN$_x$ and AlN$_x$, corrected for a 0.7 % overestimation by GGA [38]). Solid blue and black symbols are (Al,Cr)N$_{1.08}$ and (Al,Cr)N$_{1.11}$, respectively.

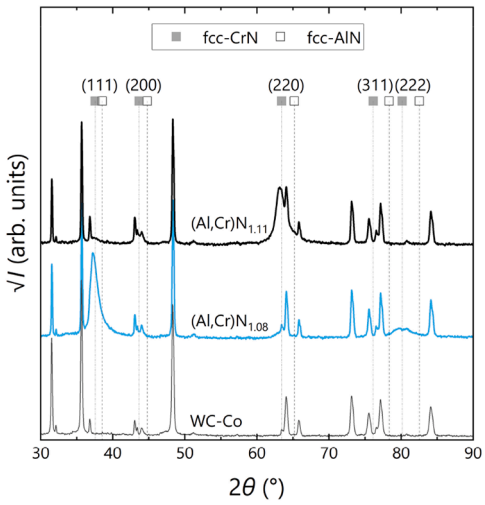

Fig. 2. X-ray diffractograms (Bragg-Brentano geometry) of the (Al,Cr)N$_{1.08}$ (blue) and (Al,Cr)N$_{1.11}$ (black) coatings on WC—Co substrates as well as that of an uncoated WC—Co substrate. The reference lines indicate the peak positions for fcc-AlN (ICDD 00–046–1200) and fcc-CrN (ICDD 01–076–2494).

2.2. Computational

The experimental investigations of superstoichiometric fcc-(Al,Cr)N$_x$ were supported by theoretical modelling of fcc-CrN$_x$ and fcc-AlN$_x$, based on the cubic NaCl-type structure (*Fm*-3*m* , #225) and using 2 × 2 × 2 conventional supercells (64 lattice sites). Lattice constants, a_0, and formation energies, E_f, for the superstoichiometric compositions were calculated as weighted averages from several symmetry inequivalent structures containing the given number of nitrogen interstitials (0–3 defects per supercell, x = 1.00–1.09) or anti-sites (0–2 defects per supercell, x = 1.00–1.13). The paramagnetic structure of fcc-CrN$_x$ was generated as quasi-random distribution of spin-up and spin-down Cr atoms (with initial local magnetic moments of ±2.3 μ_B/Cr) according to the Special Quasi-Random Structure (SQS) method [34]. In the first approximation, the effect of excess nitrogen on the lattice size of the solid solution fcc-(Al,Cr)N$_x$ can be assessed by comparing the lattice expansion rates upon increasing the concentration of nitrogen, x, (i.e. da_0/dx slopes) in fcc-CrN$_x$ and fcc-AlN$_x$ and assuming that it changes linearly with the metal fraction in the solid solution fcc-(Al,Cr)N$_x$.

Density Functional Theory (DFT) calculations were carried out employing the Vienna Ab-initio Simulation Package (VASP) [35,36] together with the projector augmented plane wave (PAW) pseudopotentials. Exchange and correlation effects were treated using the Perdew-Burke-Ernzerhof (PBE) generalised gradient approximation (GGA) [37]. The plane-wave cut-off energy was set to 500 eV, and 7 × 7 × 7 Monkhorst–Pack k-vector sampling of the Brillouin zone was used. Atomic positions and cell shapes and volumes were relaxed with 0.1 meV (per simulation box) convergence threshold for the total-energy change. Formation energies, E_f, of the individual defected materials were obtained by the equation:

$$E_f = (E_t - \sum_i n_i\mu_i)/\sum_i n_i \quad (2)$$

where E_t is the total energy, n_i is the number of atoms of species i, and μ_i is the chemical potential of atomic species i (i.e. fcc-Al, antiferromagnetic bcc-Cr, or ½N$_2$).

3. Results

In our previous study [18], we synthesised a series of (Al,Cr)N$_x$ coatings (x = 1.01–1.08, Al/(Al+Cr) = 0.59–0.62) via reactive sputtering at high power densities, without specifically addressing the distribution of excess nitrogen or the implications of superstoichiometry. Here, we extend this series to x = 1.11 (Al/(Al+Cr) = 0.63). While we discuss the full composition range (x = 1.01–1.11) to gain atomic-scale insight into nitrogen incorporation in the lattice, our microstructural and mechanical analyses primarily focus on two key compositions, (Al$_{0.62}$Cr$_{0.38}$)N$_{1.08}$ and (Al$_{0.63}$Cr$_{0.37}$)N$_{1.11}$. (For clarity, as nitrogen drives the major microstructural changes, we refer to these coatings as (Al,Cr)N$_{1.08}$ and (Al,Cr)N$_{1.11}$, respectively.)

The experimentally determined stress-free lattice parameter, a_0, shows a broadly linear increase with nitrogen concentration (see Fig. 1). However, the (Al,Cr)N$_{1.11}$ coating shows a notable deviation from this trend. To better understand the impact of nitrogen on the lattice parameter, we performed *ab initio* calculations for superstoichiometric fcc-CrN$_x$ and fcc-AlN$_x$, considering nitrogen occupying either interstitial or vacant metal sites (anti-sites). The *ab initio* results reveal that nitrogen similarly affects the lattice parameter in both superstoichiometric fcc-CrN$_x$ and fcc-AlN$_x$, with lattice expansion rates da_0/dx of 0.96±0.04 Å and 1.04±0.04 Å for interstitial sites, and −0.01±0.01 Å and 0.04±0.04 Å for anti-sites, respectively (see Fig. S1). Based on these findings, it is reasonable to assume that excess nitrogen in superstoichiometric fcc-(Al,Cr)N$_x$ would influence the lattice parameter in a similar manner. Therefore, lattice expansion in our superstoichiometric (Al,Cr)N$_x$ coatings with x up to 1.06–1.08 is likely due to nitrogen predominantly occupying interstitial sites. At higher nitrogen concentrations (x > 1.08), no further lattice expansion occurs, potentially indicating that nitrogen atoms begin to occupy anti-sites.

It is worth noting that the generalised gradient approximation (GGA) in *ab initio* calculations leads to an overestimation of the lattice constant by about 0.7 % [38]. Considering the shortcoming of GGA, the computed lattice parameter for stoichiometric fcc-(Al$_{0.6}$Cr$_{0.4}$)N$_{1.00}$—with a metal ratio closely matching that of our experiments—of 4.114 Å [39] (4.1090 Å [29]) is thus corrected to 4.085 Å (4.080 Å). This is coherent with our observations when extrapolating the experimental values back to x = 1 (see Fig. 1).

X-ray diffraction experiments in a Bragg-Brentano configuration (BBXRD) reveal that the coatings are single-phase face-centred cubic (fcc), see Fig. 2 (and Fig. S2 for GAXRD). While (Al,Cr)N$_{1.08}$ exhibits a preferred (111) growth orientation, (220) growth is favoured in (Al,Cr)N$_{1.11}$.

Cross-sectional TEM (XTEM) investigations of the (Al,Cr)N$_{1.08}$ and (Al,Cr)N$_{1.11}$ coatings are compared in Figs. 3 and 4, respectively. Both coatings initially grow with randomly oriented small grains (Figs. 3b and 4b). In (Al,Cr)N$_{1.08}$, they evolve in tightly packed, elongated fibrous

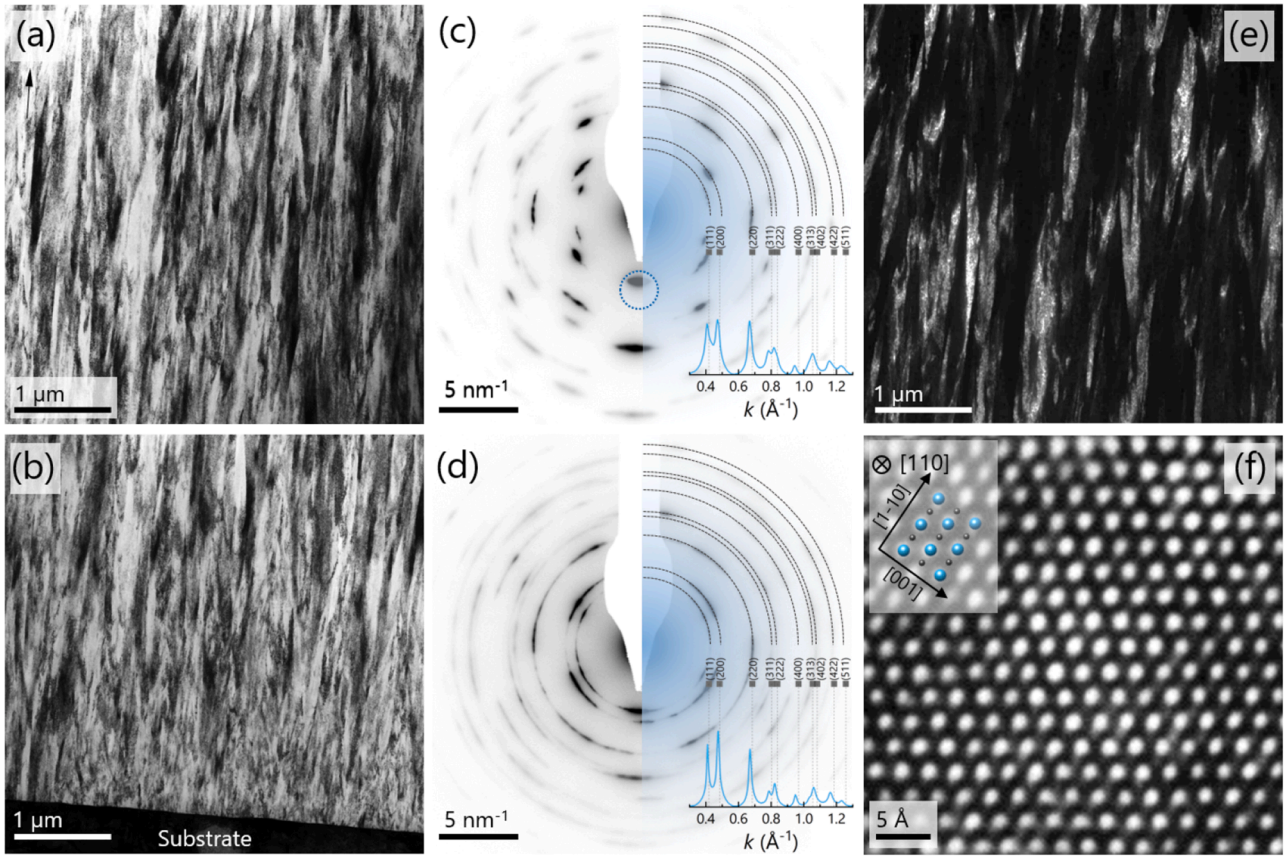

Fig. 3. Bright-field TEM images of the top (a) and bottom (b) halves of the (Al,Cr)$N_{1.08}$ coating. The corresponding SAED patterns with radially integrated intensity profiles (c) and (d), respectively. The grey lines in (c) and (d) indicate the positions obtained for a NaCl-type phase with a lattice parameter of 4.13 Å. The dark-field image (e) was obtained using an aperture over the circled region in the diffraction pattern shown in (c), with the circle indicating the approximate selection area. The HRTEM image is shown in (f). The arrow in (a) indicates the growth direction.

grains (Fig. 3a), while in (Al,Cr)$N_{1.11}$, the grains further refine and become slightly elongated in the growth direction (Fig. 4a). This is further supported by SAED patterns showing continuous diffraction rings near the substrate interface, indicating fine grains with high mosaicity in both coatings. After the initial growth stage (about 500 nm), however, the (Al,Cr)$N_{1.08}$ coating exhibits discrete diffraction spots, indicating relatively large grains, whereas the (Al,Cr)$N_{1.11}$ coating displays a continuous ring pattern, characteristic of fine grains (cf. Figs. 3c and 4c). These observations are corroborated by dark-field XTEM images (Figs. 3e and 4e).

The SAED analysis further confirms the constituent phases, as evidenced by the indexed profiles in Figs. 3c, 3d and 4c, 4d. The SAED patterns of the (Al,Cr)$N_{1.08}$ coating confirm that the coating is single-phase face-centred cubic, with diffraction in the direction of growth primarily occurring on the (111) planes (Fig. 3c, d), indicating a highly textured coating. In (Al,Cr)$N_{1.11}$, however, in addition to reflections from the fcc phase, low-intensity continuous rings indicate the presence of a hexagonal phase that is XRD-amorphous. (It is noteworthy that if the forming hexagonal phase is stoichiometric, the value of x in the cubic phase (Al,Cr)N_x should actually exceed $x = 1.11$, but not surpass 1.12, assuming the hexagonal phase fraction is <10 %. Therefore, we continue to refer to it as (Al,Cr)$N_{1.11}$.) Diffraction in the growth direction primarily occurs on the (220) planes, although the broader ring peaks compared to (Al,Cr)$N_{1.08}$ indicate a weaker texture.

Analysis of the high-resolution TEM (HRTEM) images shown in Figs. 3f and 4f reveals that the (Al,Cr)$N_{1.08}$ and (Al,Cr)$N_{1.11}$ coatings have a comparable density of dislocations in the grain interior (see Fig. S4 and S5 for the dislocation indicators superimposed on the HRTEM images). Taking into account the sessile Lomer edge dislocations which formed by two extra half planes on the intersecting planes [40,41], we obtain 7.2 × 10^{12} cm^{-2} and 8.5 × 10^{12} cm^{-2}, respectively. These are relatively high dislocation densities (compare, for instance, to 6.2 × 10^{12}–2.2 × 10^{13} cm^{-2} in CrN/AlN [42] and 2.4–4.7 × 10^{12} in TiN/AlCrN [43] superlattices). Considering that the areal dislocation density was obtained by counting the dislocations revealed by the (200), (1–11), and (−1–11) reflectors, our figures provide a lower bound on the dislocation density as some dislocation orientations do not give the contrast. The exact slip system cannot be uniquely identified from the Fourier-filtered images (Figs. S4 and S5) acquired along the [110] direction; the commonly observed closure loop vector in the image plane, $a/4$[11–2], is consistent with the projection of an $a/2$[110] Burgers vector, where a is the cubic lattice parameter.

Nanoindentation measurements, Fig. 5, reveal that the (Al,Cr)$N_{1.08}$ and (Al,Cr)$N_{1.11}$ coatings exhibit hardness, H, values of 34.4 ± 2.9 GPa and 31.6 ± 2.1 GPa, respectively, averaged over penetration depths of 0.2 to 0.5 μm. Extrapolation of the indentation modulus data for penetration depths greater than 0.2 μm back to zero penetration yields modulus, E, values of 467±27 GPa and 373±20 GPa, respectively. The hardness of both (Al,Cr)$N_{1.08}$ and (Al,Cr)$N_{1.11}$ falls within the range 30–36 GPa measured for all superstoichiometric compositions in our previous study [18]. The elastic modulus of (Al,Cr)$N_{1.08}$ is also consistent with the range of the superstoichiometric compositions 460–480 GPa, whilst E of (Al,Cr)$N_{1.11}$ is strikingly low.

For the micropillar splitting tests, the nanoindentation results were used to assess the gamma coefficients (Fig. S6). The (Al,Cr)$N_{1.08}$ and (Al,Cr)$N_{1.11}$ coatings exhibit fracture toughness values (K_C) of 3.80±0.19 and 4.15±0.13 MPa$\sqrt{m}$, respectively (Fig. 6). For comparison, benchmark industrial cathodic arc evaporation (Al,Cr)N coating with a similar

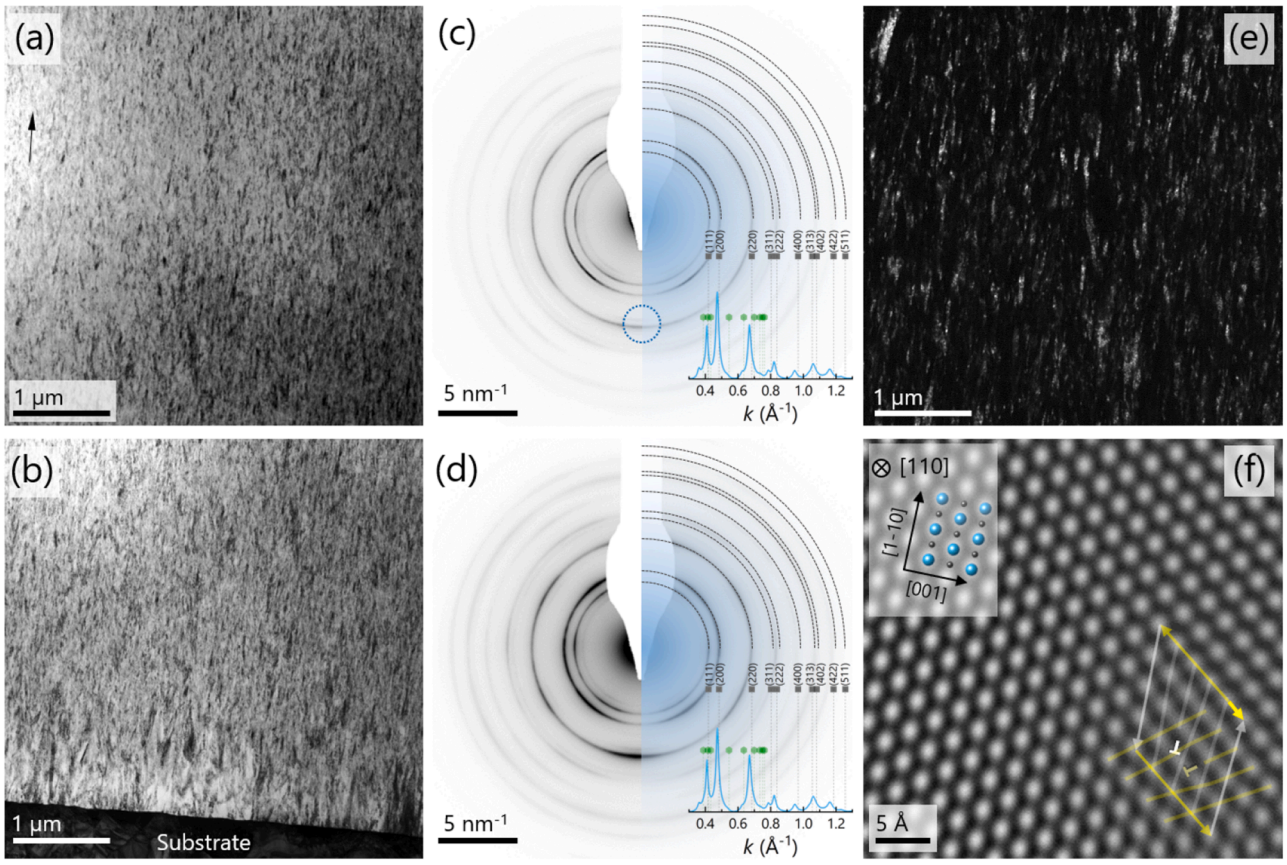

Fig. 4. Bright-field TEM image of the top (a) and bottom (b) halves of the (Al,Cr)$N_{1.11}$ coating. The corresponding SAED patterns with radially integrated intensity profiles (c) and (d), respectively. The grey lines in (c) and (d) indicate the positions obtained for a NaCl-type phase with a lattice parameter of 4.13 Å. The green lines for low-intensity reflections from a second phase are based on w-AlN powder diffraction data (ICSD 34475). The dark-field image (e) was obtained using an aperture over the circled region in the diffraction pattern shown in (c), with the circle indicating the approximate selection area. The HRTEM image is shown in (f). The arrow in (a) indicates the growth direction.

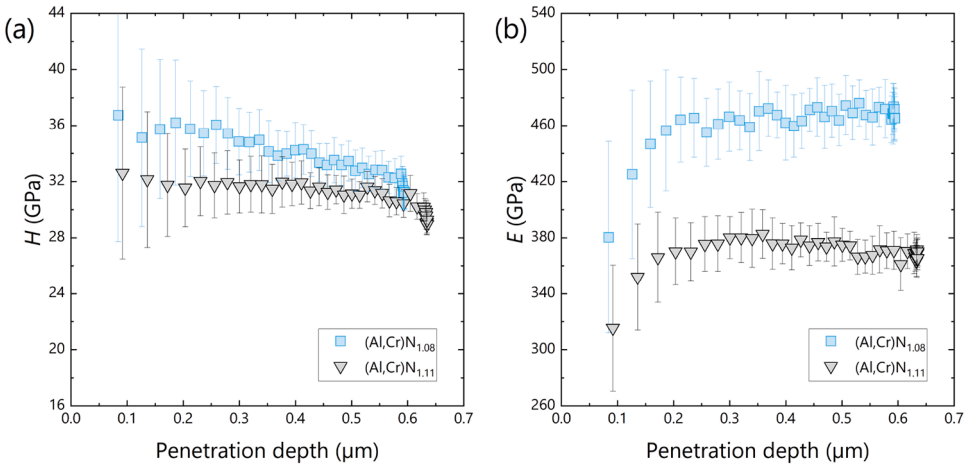

Fig. 5. Depth-resolved nanoindentation hardness (a) and modulus (b) of the (Al,Cr)$N_{1.08}$ and (Al,Cr)$N_{1.11}$ coatings deposited on WC substrates; error bars represent standard deviations from 12 measurements.

Al/(Al+Cr) ratio has an average K_C of 3.73±0.50 MPa$\sqrt{m}$ [18]. The load-displacement curves and SEM images show the typical fracture of the micropillars for each coating. We note that K_C was effectively the same regardless of whether the pillar underwent a 3-way or a 2-way split upon the initial load drop following maximum load, as we commented previously [18].

In the cutting tests, varied performance outcomes were observed, with the (Al,Cr)$N_{1.08}$ coating demonstrating the highest wear resistance in the end milling test, while the (Al,Cr)$N_{1.11}$ coating exhibited superior performance in the fly cutting test. In the end milling test, after removing 2500 cm^3 of the tool steel, the end mills coated with (Al,Cr)$N_{1.08}$ show lower wear than those coated with (Al,Cr)$N_{1.11}$, compare 13±10 μm and 37±6 μm (major edge) and 28±6 μm and 43±5 μm (minor edge), respectively, see Fig. 7a. Both coatings show greater wear

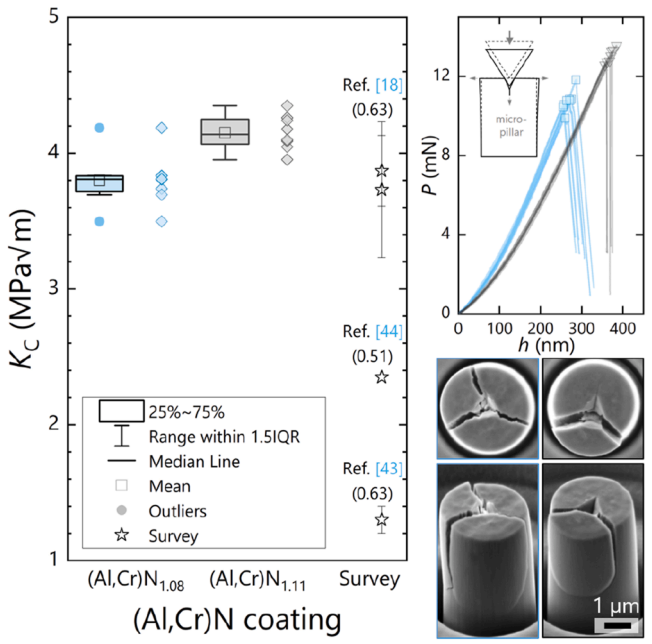

Fig. 6. Box plot of fracture toughness for the $(Al,Cr)N_{1.08}$ and $(Al,Cr)N_{1.11}$ coatings, with individual micropillar values shown on the right. Literature comparison of available (Al,Cr)N fracture toughness data, with Al/(Al+Cr) ratios in brackets [18,43,44]. Also shown are load-displacement (*P-h*) curves and SEM images of the fractured micropillars (top and side views).

resistance than the benchmark CAE coating, with wear measuring 33±4 μm at the major edge and 50±6 μm at the minor edge [18]. In the fly cutting test, which simulates the performance of the coating in a gear hobbing application [45], the $(Al,Cr)N_{1.08}$ and $(Al,Cr)N_{1.11}$ coatings demonstrated wear resistance of 5 and 6 m/tooth, respectively. It is worth noting that the tool life depends strongly on the coating thickness. For example, increasing the coating thickness by about 50 % nearly doubles the tool life (Fig. 7b).

For clarity, the key results for the $(Al,Cr)N_{1.08}$ and $(Al,Cr)N_{1.11}$ coatings are summarised in Table 1. This table presents a consolidated overview of the elemental concentrations, stress-free lattice parameters, growth orientations, nanoindentation hardness and modulus values, and residual stresses for both coatings.

4. Discussion

4.1. Superstoichiometry

The effect of light elements on the structure-property relationships of ceramic materials is frequently left out of discussions, largely due to the limitations of available measurement techniques in accurately determining their concentration. The widely employed energy-dispersive X-ray spectroscopy (EDS), for instance, lacks accuracy due to the low fluorescence yield of light elements [46]. Although light element calibration standards might substantially reduce measurement uncertainties, careful verification remains essential. For example, additionally analysing lattice parameters can offer critical insights (provided that other contributing factors, such as residual stresses, are carefully accounted for and excluded). Here, nitrogen concentration was assessed via EDS calibrated with a CrN standard and the difference in nitrogen concentration in $(Al,Cr)N_{1.08}$ and $(Al,Cr)N_{1.11}$ was confirmed using ERDA. Combined with stress-free lattice parameter measurements and *ab initio* calculations, our results unequivocally demonstrate that the coatings are superstoichiometric (i.e., the nitrogen-to-metal atomic ratio exceeds 1).

Various factors may contribute to the formation of superstoichiometric compositions. One such cause is the occupation of interstitial sites by non-metal atoms. Vacant metal sites also lead to superstoichiometry, while their occupation by non-metal atoms (antisite defects) can further amplify this effect. In polycrystalline films, grain boundaries can act as sinks for excess nitrogen, providing short diffusion paths to the growth surface [47]. Another potential mechanism is a phase transition, such as from the NaCl-type structure to a nitrogen-rich

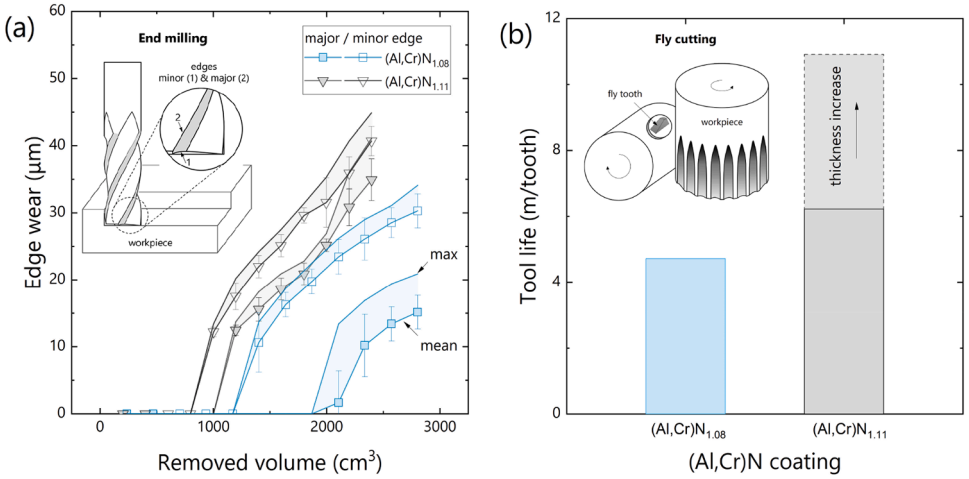

Fig. 7. Wear resistance of the $(Al,Cr)N_{1.08}$ and $(Al,Cr)N_{1.11}$ coatings in the end milling (a) and fly cutting (b) tests. In the end milling test, the mean and maximum wear were measured for both, the major (solid symbols) and minor (open symbols) cutting edges, as depicted schematically in the illustration.

Table 1
Elemental concentration, stress-free lattice parameters, a_0, texture, nanoindentation hardness, *H*, and modulus, *E*, and residual stress, σ, for the $(Al,Cr)N_x$ coatings with $x = 1.08$ and 1.11.

x	N, at. %	Al/(Al+Cr)	a_0, Å	Texture	*H*, GPa	*E*, GPa	-σ, GPa	K_C, MPa√m
1.08	52.0 ± 0.1	0.62	4.1318±0.0080	(111)	34.4 ± 2.9	467±27	4.3 ± 0.6	3.80±0.19
1.11	52.5 ± 0.1	0.63	4.1296±0.0027	(220)	31.6 ± 2.1	373±20	4.6 ± 1.0	4.15±0.13

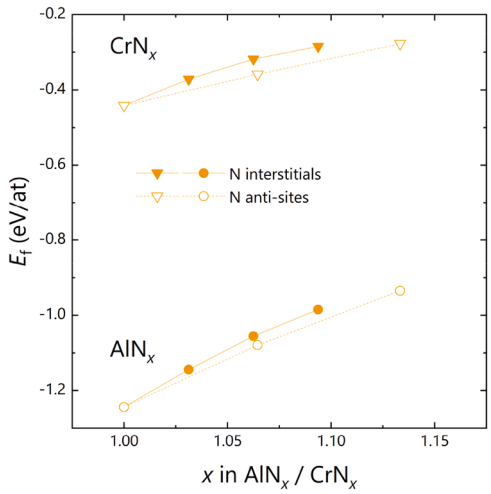

Fig. 8. Formation energies of superstoichiometric fcc-CrN_x and fcc-AlN_x with N atoms occupying interstitial and anti-sites.

phase like the CaF_2-type structure containing up to two nitrogen atoms per metal atom [48].

Our observations show that an increase in nitrogen concentration correlates with lattice expansion, making the formation of metal vacancies unlikely. Furthermore, no phase transformation to a CaF_2-type structure was observed. Therefore, nitrogen atoms incorporated into the lattice appear to be the primary cause of the lattice expansion.

Excess nitrogen in the coatings results from energetic deposition. A high plasma density enhances nitrogen ionisation near the target, leading to an increased density of N_2^+ ions. These ions accelerate toward the target and dissociate upon impact with the target atoms (provided their energy exceeds greatly the bond energy of 9.8 eV [49]). They can be backscattered by the heavier metal atoms as energetic neutral atoms [50–52] and subsequently subplanted into the growing coating. This reasoning is further corroborated through a series of experiments with a stronger magnetic field [18], which enhances electron confinement, increasing the probability of N_2 and Ar ionisation through collisions. As a result, plasma density rises, leading to a higher flux of energetic backscattered neutrals [53], reinforcing the incorporation of excess nitrogen.

Although lattice expansion in superstoichiometric nitrides has been previously observed in (Al,Cr)N [54] and other metal nitrides [55–58], with some studies suggesting it arises from energetic nitrogen atoms backscattered from the target [56–58], the specific lattice sites occupied by the excess nitrogen in these compounds remain largely unresolved. Excess nitrogen atoms can occupy interstitial sites, precisely tetrahedral voids, and even form N dimers, with (111) split being most probable [59–61], or vacant metal sites (anti-sites).

Although from the formation energy point of view, nitrogen atoms are expected to occupy metal vacant sites (see Fig. 8), under conditions of energetic bombardment with energetic backscattered neutrals interstitial sites might become preferable. Indeed, our experimental and computational results provide compelling evidence that superstoichiometric fcc-CrN_x and fcc-AlN_x—and likely in fcc-$(Al,Cr)N_x$ as well—form primarily due to incorporation of nitrogen into interstitial lattice sites. Up to x of about 1.06–1.08, the excess nitrogen induces lattice expansion, similar to its effect on interstitial sites observed in *ab initio* calculations (Fig. 1).

The reason for the deviation from the lattice expansion rate predicted by *ab initio* calculations can be twofold. First, the increase in aluminium concentration with increasing nitrogen content counteracts the lattice expansion caused by nitrogen occupying interstitial sites. Specifically, an increase in the Al/(Al+Cr) ratio from 0.59 to 0.63 reduces the lattice parameter of stoichiometric (Al,Cr)N by about 0.004 Å, as interpolated from *ab initio* calculations [39] (approximately one-tenth the magnitude of the lattice expansion observed experimentally). Second, nitrogen atoms can also occupy the anti-sites (vacant metal lattice sites). The normalised nitrogen fraction x of about 1.06–1.08 appears to be a solubility limit of nitrogen at the interstitial sites, as higher concentrations of nitrogen do not cause any further expansion of the crystal lattice but can significantly elevate the re-nucleation rate of grains disrupting columnar growth.

4.2. Microstructure

The $(Al,Cr)N_{1.08}$ and $(Al,Cr)N_{1.11}$ coatings show a dense microstructure. This is primarily attributed to the high degree of ionisation of sputtered particles [18,62] achieved through the peak power densities characteristic of the HiPIMS process [19–21]. High momentum transfer during intense ion bombardment leads to higher nucleation rates and density of the coatings [63,64]. As a result, most of the coatings including $(Al,Cr)N_{1.08}$ have tightly packed elongated fibrous grains, while $(Al,Cr)N_{1.11}$ has much smaller grains and the columnar growth is hindered indicating a much higher re-nucleation rate. The $(Al,Cr)N_{1.08}$ coating is (111) oriented, similar to all coatings with $x < 1.08$ [18], while the $(Al,Cr)N_{1.11}$ exhibits (110) growth. Hence it can be anticipated that exceeding the solubility limit of nitrogen at the interstitial sites ($x >$ 1.06–1.08) results in change of the direction of the preferential growth. (Note that in this section, we refer to the low-index planes (100) and (110) instead of the XRD reflections (200) and (220), which are commonly used elsewhere in the manuscript, to discuss surface energy and growth orientation.)

The development of preferential orientation in PVD metal nitrides is influenced by the intricate interplay of kinetic and thermodynamic factors. While these mechanisms are well-established and extensively studied for TiN and (Al,Ti)N, they have been less explored for CrN, and even less so for (Al,Cr)N. As a result, discussions on preferential growth in (Al,Cr)N often draw on insights from studies of TiN and (Al,Ti)N.

According to thermodynamic considerations, the grain growth direction is governed by the competition between surface and strain energies [65,66]. In both TiN [67] and CrN [68], the (100) plane has the lowest surface energy, making it the preferred orientation during initial growth. However, with increasing thickness, the accumulation of compressive stress leads to a shift in preferred orientation toward planes with lower in-plane strain energy. Since the in-plane Young's modulus of TiN [69] and CrN [29] is lower for (111) compared to (100), thicker coatings tend to develop a (111) preferred orientation.

Ab initio calculations for TiN and (Al,Ti)N further refine this understanding by introducing the concept of surface chemical potential, μ, as a decisive factor in growth orientation [70]. The chemical potential of the (111) plane in TiN is lower than that of the (100) plane, resulting in the migration of Ti adatoms from (100) to (111) surfaces and hence favouring (111) growth. The chemical potential advantage for (111) growth decreases, however, upon alloying with AlN. (Additionally, alloying with AlN reduces the mobility of Al and Ti adatoms on the (111) and (100) surfaces near substituted Al atoms, respectively [67,71], leading to (111)-oriented grains enriched in Al and (100)-oriented grains enriched in Ti.)

However, experimental studies soon demonstrated that kinetic factors can play an equally significant if not even dominant role in determining growth orientation [72,73]. It has been shown that by controlling ion energy, E_i, and—to a considerably greater extent—the incident ion-to-metal-atom flux ratio, J_i/J_{Me}, (100) growth can be favoured even in the presence of compressive residual stresses [72,73]. In fact, while low E_i and J_i/J_{Me} result in low momentum transfer upon collisions with the surface atoms and therefore low adatom mobility, promoting (111) growth, high E_i and particularly J_i/J_{Me} result in increased adatom mobility and favour (100) growth, e.g. in TiN and (Al,Ti)N [56,57,74]. Adatom mobility can also be affected by the homologous temperature, $T_h = T_s/T_m$ (with T_s and T_m being substrate

temperature and melting point, respectively), and is the higher, the higher the T_s and the lower the T_m. In (Al,Ti)N, T_h increases with AlN content, as AlN has a lower melting point than TiN, promoting (100) growth [75]. And conversely, in (Al,Mo)N or (Al,Cr)N, T_h decreases with AlN content due to a higher melting point of AlN compared to $MoN_{0.5}$ and CrN, limiting adatom mobility and favouring (111) growth [17].

Together, these considerations converge on the prediction of a (100) preferential orientation in our coatings. Thermodynamically, (100) growth is favoured for the experimentally obtained $(Al_{0.62}Cr_{0.38})N$ composition (yet a stoichiometric composition) as $E_{100}<E_{110}<E_{111}$ [29]. Kinetically, high E_i and J_i/J_{Me} ratios enhance adatom mobility, which is expected to be higher than in (Al,Ti)N—for the same mole fraction of AlN—due to the lower melting point of CrN compared to TiN, further supporting (100) growth. However, the $(Al,Cr)N_{1.08}$ coating, as well as those with $x < 1.08$ [18], despite being deposited under high J_i/J_{Me} or high E_i (bias voltage up to 150 V), exhibit a strong (111) preferential orientation. The (111) preferential growth of (Al,Cr)N under high J_i/J_{Me} or E_i has also been observed previously [76–80].

Alongside momentum transfer, the density of atomic nitrogen or collisionally dissociating N_2^+ in the total ion flux J_i/J_{Me} can significantly influence the growth kinetics, as shown for TiN [70]. An increased flux of atomic N or N_2^+ reduces the chemical potential on the (100) surface, while having minimal impact on the (111) surface, as nitrogen does not chemisorb on the N-terminated (111) surface [70]. If the flux is sufficiently high, the surface potential on the (100) surface can drop below that on the (111) surface, thereby favouring (100) growth. Assuming that the surface chemical potential in CrN behaves similarly to TiN, the nitrogen surface coverage under the deposition conditions leading to $x <$ 1.08 appears insufficient in lowering the chemical potential of metal adatoms on the (100) surface, thereby failing to promote (100) growth. The high density of atomic N backscattered from the target becomes subplanted rather than chemisorbed at the surface. Consequently, diffusivity is likely higher on the (100) surface compared to the (111), promoting the preferential growth of (111)-oriented grains.

The surface energy of (110) in TiN is nearly twice that of the (100) and (111) surfaces, making it the least energetically favourable among the three low-index surfaces. In CrN, (111) has the highest surface energy among the low-index planes, while the surface energy of (110) is still nearly twice that of (100) [68]. Alloying TiN with AlN has only little effect on adatom mobility [67]. Although no studies have specifically examined the effect of AlN addition on adatom mobility in CrN, it can be anticipated that (110) growth remains thermodynamically unfavourable in (Al,Cr)N as well.

In PVD coatings, (110) growth is commonly observed at high E_i, e.g. by using high bias voltage, as seen in TiN [81–83] and CrN [84,85]. Similar to fcc metals with the <110> direction of the minimum loss of energy of the impinging ions, the (110) surface is less prone to resputtering by energetic ions compared to the densest (100) and N-terminated (111) surfaces. This "ion channelling" is likely driven by a significantly higher flux of energetic backscattered nitrogen atoms compared to other coatings. However, (110) has also been observed at relatively low bias voltages, yet under high nitrogen partial pressures and low temperatures [86–90] or high temperatures [91]. Therefore, in addition to "ion channelling", other factors may also contribute to the (110) growth orientation. The excess nitrogen atoms within the (110)-oriented grains may occupy interstitial sites along the ⟨110⟩ direction with a local CaF_2 lattice arrangement (yet not a CaF_2-type phase) [92,93].

4.3. Mechanical properties

4.3.1. Hardness and Young's modulus

The hardness of $(Al,Cr)N_{1.08}$ is 9 % higher than that of $(Al,Cr)N_{1.11}$, compare 34.4 ± 2.9 GPa and 31.6 ± 2.1 GPa, respectively. Such high hardness has been attributed to the fully dense grain boundaries (GBs) and a high concentration of defects obstructing dislocation motion [1,10,94,95]. Of particular importance in superstoichiometric coatings are nitrogen atoms occupying interstitial sites and exerting strains on the surrounding lattice. Both, high atomic density of GBs and high concentration of defects are achieved by bombardment with the energetic ions and neutrals backscattered from the target. The lower hardness of $(Al,Cr)N_{1.11}$, despite the expected strengthening effects from grain refinement, is likely due to the presence of anti-site defects or the formation of the hexagonal phase.

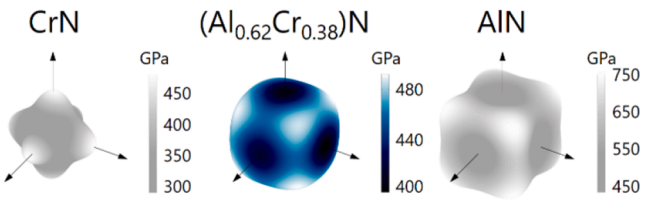

Fig. 9. Elastic moduli anisotropy in a stoichiometric fcc-$(Al_{0.62}Cr_{0.38})N$ based on the weighted average of the c_{ij} components for metal ratios Al/(Al+Cr) between 0.56 and 0.67 reported in Ref. [29].

The $(Al,Cr)N_{1.08}$ coating has a 25 % higher stiffness than $(Al,Cr)N_{1.11}$, compare 467±27 GPa and 373±20 GPa, respectively. The other superstoichiometric compositions with (111) preferential growth are within the range 460–500 GPa. Particularly striking is thus the low Young's modulus of the $(Al,Cr)N_{1.11}$ coating. Changes in the bonding character upon increasing the defect concentration cannot solely account for the difference (compared to the changes in E values, which range from 460 to 500 GPa for x between 1.01 and 1.08 [18]). Additionally, calculations of the directional Young's moduli, based on the weighted average of the elastic c_{ij} components of stoichiometric (Al,Cr)N for metal ratios Al/(Al+Cr) between 0.56 and 0.67 [29], yield values of E_{111} = 474 GPa, E_{110} = 463 GPa, E_{100} = 402 GPa (see Fig. 9). Consequently, a change in preferential growth orientation from (111) to (220) is expected to have only a minor influence on the nanoindentation modulus, although directional differences in elastic response may become more pronounced in superstoichiometric compositions. Other factors, such as grain boundaries, can also play a substantial role. Their volume fraction is considerably higher in fine-grained coatings, and due to their lower atomic coordination and packing density, GBs can reduce the overall stiffness. Furthermore, the presence of the hexagonal phase and anti-site defects could further contribute to the reduction of Young's modulus in $(Al,Cr)N_{1.11}$.

4.3.2. Fracture toughness

The $(Al,Cr)N_{1.08}$ and $(Al,Cr)N_{1.11}$ coatings exhibit fracture toughness values (K_C) of 3.80±0.19 and 4.15±0.13 MPa$\sqrt{m}$, respectively (Fig. 6). Fracture toughness of sputter-deposited (Al,Cr)N coatings assessed in cantilever bending tests (K_{IC}) varies from 2.35 MPa$\sqrt{m}$ (for Al/(Al+Cr) of 0.51, A. Drnovšek et al. [44]) to 1.3 MPa$\sqrt{m}$ (for Al/(Al+Cr) of 0.63, J. Buchinger et al. [43]). In our recent study [18], sputter-deposited and cathodic arc evaporated coatings showed pillar splitting fracture toughness of 3.87±0.26 and 3.73±0.50 MPa$\sqrt{m}$.

To draw a comparison between the results obtained using both measurement methods, several aspects need to be considered. On the one hand, Ga ions implanted in the notch during the FIB milling process are likely to affect fracture toughness in a single-cantilever bending tests. In contrast, in micropillar splitting tests, the initial sub-critical cracks generate in a region being largely unaffected by the FIB milling process, although experiments on micropillars of single-crystal Si have shown that the FIB milling might cause a few tens of nm amorphisation with implanted Ga ions resulting ultimately in higher apparent fracture toughness [96].

In a comparative study on CrN coatings [97], fracture toughness determined in a single-cantilever bending test was found to be systematically higher than in micropillar splitting tests. The plausibility of our results is furthermore corroborated by the solid solution toughening

effect caused by an addition of aluminium. Comparing the fracture toughness of our (Al,Cr)N coatings with CrN having 2.95±0.23 MPa$\sqrt{m}$ [97], solid solutions (Al,Cr)$N_{1.08}$ and (Al,Cr)$N_{1.11}$ exhibit 29 % and 41 % higher fracture toughness, respectively. An (Al,Ti)N coating with a similar Al/(Al+Ti) ratio has a 42 % higher fracture toughness than TiN, compare 2.7 MPa$\sqrt{m}$ and 1.9 MPa$\sqrt{m}$ [98].

The inherent brittleness of ceramics at low temperatures stems from the ease of crack nucleation and propagation. Crack nucleation can be facilitated by pre-existing micropores, which concentrate stress, while crack propagation is facilitated by a lack of significant energy dissipation by plasticity. In the PVD coatings, however, fracture commonly occurs along the GBs which have a lower fracture resistance than the grain interior [99–101]. Accordingly, cracks in the coatings with a columnar microstructure would traverse the entire thickness. The dense, cohesive GBs expected from energetic deposition, and their more convoluted arrangement in the fine-grained, (220)-textured (Al,Cr)$N_{1.11}$, may explain the toughness improvement. Furthermore, the high initial dislocation densities may additionally serve as a defect source for mediating some plasticity in these dense face-centred cubic nitrides by Peierls stress-controlled slip on the {111} or {110} planes along <1 − 10> or <11−2> directions [1,41,102].

Accordingly, our coatings might indeed have a higher fracture toughness than any other sputter-deposited monolithic (Al,Cr)N coatings investigated previously. Further fracture toughness enhancement is envisioned: engineering the GB distribution (e.g. through the grain nucleation rate via N_2 process pressure) to enable crack deflection or hinder crack propagation is effective for energy dissipation [103,104]. Such control of cracking is widely used to improve fracture toughness, for instance, by activating delamination toughening [105], twisting and tilting columnar grains [106–109], in multilayers and superlattices [110–112], and combination thereof [113]. Another strategy would be to further increase the dislocation density to achieve greater crack shielding through dislocation activity, as seen in TiN [114], and by defect engineering, e.g. to facilitate twinning-induced plasticity [115].

4.4. Wear resistance

The (Al,Cr)$N_{1.08}$ coating exhibits superior wear resistance in the end milling tests (185 % and 54 % on major and minor edges, respectively). Being 9 % (or 2.8 GPa) harder than the (Al,Cr)$N_{1.11}$ coating, superior resistance against abrasive wear can be anticipated. However, harder coatings do not always outperform softer coatings in end milling, and other fundamental mechanisms play an important role in the overall performance of the coating [18]. For example, growth-induced compressive residual stresses help in inhibiting crack propagation, and ultimately lower wear rates, by diminishing crack tip stresses. This is why higher nitrogen pressures during the deposition process commonly lead to lower wear rates [18,116]. However, it is evident that after a critical concentration of interstitial atoms is achieved, further increase in nitrogen pressure leads to considerable changes of the microstructure without great changes in compressive stresses, compare 4.3 and 4.6 GPa for (Al,Cr)$N_{1.08}$ and (Al,Cr)$N_{1.11}$, respectively. Also, the (Al,Cr)$N_{1.08}$ coating performs better than the (Al,Cr)$N_{1.11}$ coating despite being about 8 % more brittle. Finally, the presence of the hexagonal w-AlN in the (Al,Cr)$N_{1.11}$ coating can negatively affect the resistance against abrasive wear [117].

The (Al,Cr)$N_{1.11}$ coating exhibits superior performance in the fly cutting test. Here, crater wear typically initiates on the trailing flank of the fly cutting tooth, progresses to the leading flank, and crater wear emerges on the cutting face [33]. Crater wear near the edge of the cutting faces affects the wear on the leading flank, potentially limiting the overall lifetime of the tool. It is evident from interrupted testing, where only one gear tooth was cut, that the crater wear in (Al,Cr)$N_{1.11}$ is substantially reduced, see Fig. 10. Crater wear is caused by large chip thicknesses. Such large chip thicknesses apply higher load on the cutting face, causing a higher thermal and abrasive impact. In terms of the

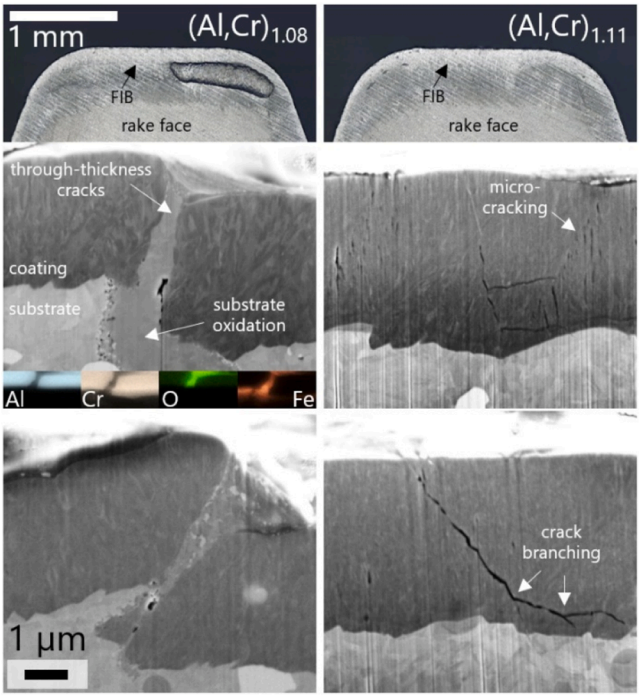

Fig. 10. SEM images of the tools coated with (Al,Cr)$N_{1.08}$ and (Al,Cr)$N_{1.11}$ after cutting one gear tooth, along with FIB cross-sections of the not-yet-cratered regions, and associated EDS chemical mapping of in-/egress material where relevant.

sub-surface cracking, extensive through-thickness cracking was observed in the not-yet-cratered region in the (Al,Cr)$N_{1.08}$; this is associated with vertical or inclined shearing of the coating and oxygen ingress along the cracks evidenced by back-filling with iron oxide from the HSS substrate, identified by EDS mapping. In contrast, cracking in the (Al,Cr)$N_{1.11}$ generally does not reach the substrate, deviating horizontally instead.

Factors responsible for improved crater wear resistance are extensive microcracking instead of few, major cracks, as well as a higher fracture toughness, and likely beneficial crystallographic orientation of the coating [118]: for example, for CVD TiN coatings, (220) orientation was shown to be advantageous in postponing the onset of crater wear and decreasing the rate of crater formation. Further factors in wear likely affect both coatings equivalently; in brief, these are: substrate-coating and coating-workpiece chip adhesion, smoother coating surfaces from fewer growth defects reducing wear rate [119,120], so-called geometric antennae effects of coating deposition whereby microstructure and composition at the cutting edge differ from those far from the edge, where measurements are commonly made (as here) [121,122]. Finally, under the dry-cutting conditions here, friction-induced heating in the contact zone between the tool and chip can exceed the tempering temperature of the HSS tool, lead to its softening and hence loss of load bearing capacity, which accelerates the wear process [123,124]. A lower out-of-plane component of thermal conductivity to reduce heat transmission to the substrate, and higher in-plane thermal conductivity effective for heat dissipation across the coating is considered paramount for HSS protection and thereby increased tool life. These conductivity properties and the effect of the microstructure have not yet been well ascertained for the present coatings.

The semi-empirical criteria H/E (elastic strain to failure [125]) and H^3/E^2 (resistance to plastic deformation [126]) are commonly used to predict the fracture toughness and wear resistance of the coatings [125, 127]. Our results demonstrate that opposite outcomes might be obtained from different cutting tests, making it impossible to generalise conclusions about wear resistance predictions. As for the fracture toughness,

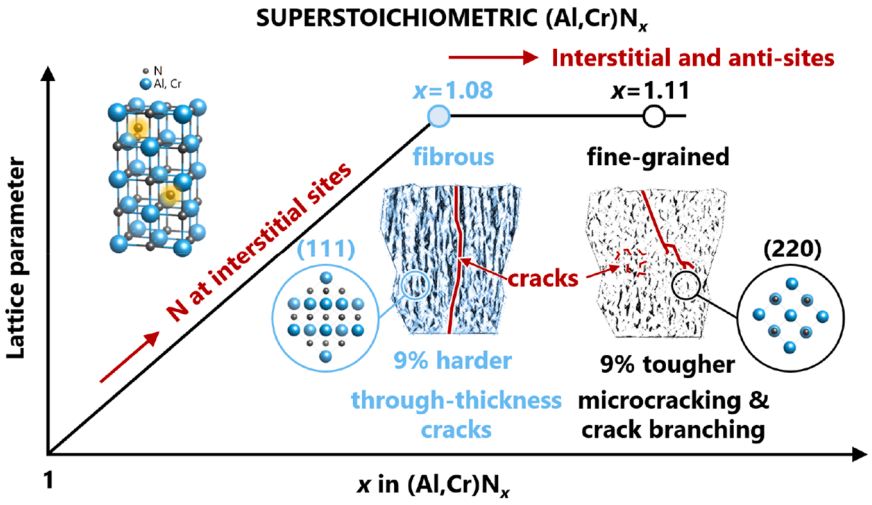

Fig. 11. Mechanistic interpretation of the superstoichiometry and properties of (Al,Cr)N_x coatings.

both criteria can lose their predictive accuracy when there are substantial changes in the microstructure [128,129]. In this study, however, the (Al,Cr)$N_{1.08}$ and (Al,Cr)$N_{1.11}$ coatings—despite having a 0.5 at. % difference in N concentration but substantially different microstructures—have H/E of 0.074±0.011 vs. 0.085±0.010, and H^3/E^2 of 0.19±0.07 GPa vs. 0.23±0.07 GPa, respectively, thus correctly predicting higher toughness of the (Al,Cr)$N_{1.11}$ coating.

Both coatings are highly effective in prolonging the tool life. Yet to fully harness the potential of high-performance tools, coatings should be tailored to suit specific applications. The wear mechanisms activated during interrupted cutting processes, such as fly cutting or end milling, which involve cyclic impact and resultant thermal shock, are complex. This section highlights several important aspects that influence the wear resistance of the superstoichiometric coatings studied; however, the aspects discussed here are not comprehensive. This complexity also presents challenges in developing semi-empirical criteria for predicting wear behaviour based on the room-temperature hardness, Young's modulus, and fracture toughness. Further investigations at cutting temperatures and under loading conditions equivalent to those at the cutting edge are needed to link the performance of wear-resistant coatings with their lab-measured micro/nano-mechanical properties.

5. Conclusions

By employing high-ionisation magnetron sputtering (HIMS), which generates a high flux of ions and energetic neutrals, we recently synthesised a series of (Al,Cr)N_x coatings with x ranging from 1.01 to 1.08 and similar Al/(Al+Cr) ratios (0.59–0.62), without addressing the distribution of excess nitrogen or the effects of superstoichiometry. In the present study, we extended the x range to 1.11 and, by integrating elemental concentrations, stress-free lattice parameters, and *ab initio* calculations, identified the locations of excess nitrogen atoms with a high degree of confidence. Below a threshold concentration of about $x \approx$ 1.06–1.08, excess nitrogen primarily occupies interstitial lattice sites, whereas beyond this threshold, it can also incorporate into vacant metal sites (anti-sites).

A detailed investigation was conducted on two superstoichiometric (Al,Cr)N_x coatings: (Al,Cr)$N_{1.08}$, with nitrogen concentration near the threshold, and (Al,Cr)$N_{1.11}$, with a concentration above it. While (Al,Cr)$N_{1.08}$ has tightly packed, elongated fibrous grains with a strong (111) growth orientation, (Al,Cr)$N_{1.11}$, due to a significantly increased rate of grain re-nucleation, develops a fine-grained microstructure with a (220) growth orientation. These structural differences have a pronounced impact on mechanical properties, as summarised in Fig. 11. While (Al,Cr)$N_{1.08}$ is 9 % harder (34.4 GPa vs. 31.6 GPa) and demonstrates superior abrasive resistance and performance in end milling tests, (Al,Cr)$N_{1.11}$ exhibits 9 % higher fracture toughness (4.15 MPa$\sqrt{m}$ vs. 3.80 MPa$\sqrt{m}$) and enhanced microcracking and crack-branching behaviour, which is beneficial for impact applications such as gear hobbing. Our results not only underscore the advantages of superstoichiometric (Al,Cr)N coatings but also suggest a broader potential for superstoichiometric nitrides and ceramics in advanced applications.

Data availability

The raw/processed data required to reproduce these findings cannot be shared at this time as the data also forms part of an ongoing study.

CRediT authorship contribution statement

F.F. Klimashin: Writing – original draft, Visualization, Supervision, Project administration, Methodology, Investigation, Formal analysis, Data curation, Conceptualization. **M. Učík:** Writing – review & editing, Methodology, Investigation, Formal analysis, Data curation. **M. Matas:** Writing – review & editing, Validation, Methodology, Investigation, Formal analysis, Data curation. **D. Holec:** Writing – review & editing, Validation, Methodology, Investigation, Formal analysis, Data curation. **M. Beutner:** Writing – review & editing, Validation, Methodology, Investigation, Formal analysis, Data curation. **M. Hackert-Oschätzchen:** Writing – review & editing, Methodology. **A. Xomalis:** Writing – review & editing, Validation, Methodology, Investigation, Formal analysis. **J.J. Schwiedrzik:** Writing – review & editing, Methodology. **J. Klusoň:** Writing – review & editing, Methodology. **M. Jílek:** Methodology. **A. Lümkemann:** Writing – review & editing, Supervision, Resources, Project administration, Methodology, Funding acquisition, Formal analysis, Conceptualization. **J. Michler:** Writing – review & editing, Supervision, Resources, Project administration, Funding acquisition, Formal analysis, Conceptualization. **T.E.J. Edwards:** Writing – review & editing, Supervision, Resources, Project administration, Methodology, Investigation, Funding acquisition, Formal analysis, Data curation.

Declaration of competing interest

The authors declare that they have no known competing financial interests or personal relationships that could have appeared to influence the work reported in this paper.

Acknowledgments

This research was supported by the Innosuisse Project 42220.1 IP-ENG. The authors acknowledge Dr. Arnold Müller and Dr. Christof Vockenhuber for conducting the ERDA experiments.

Supplementary materials

Supplementary material associated with this article can be found, in the online version, at doi:10.1016/j.actamat.2025.121158.

References

[1] L. Toth, Transition metal carbides and nitrides, (1971).
[2] F.F. Klimashin, N. Koutna, H. Euchner, D. Holec, P.H. Mayrhofer, The impact of nitrogen content and vacancies on structure and mechanical properties of Mo-N thin films, J. Appl. Phys. 120 (18) (2016) 185301.
[3] M. to Baben, L. Raumann, D. Music, J.M. Schneider, Origin of the nitrogen over- and understoichiometry in Ti(0.5)Al(0.5)N thin films, J. Phys. Condens. Matter. 24 (15) (2012) 155401.
[4] D. Holec, L. Zhou, Z. Zhang, P.H. Mayrhofer, Impact of point defects on the electronic structure of paramagnetic CrN, arXiv preprint arXiv:1410.0758 (2014).
[5] S.H. Jhi, J. Ihm, S.G. Louie, M.L. Cohen, Electronic mechanism of hardness enhancement in transition-metal carbonitrides, Nature 399 (6732) (1999) 132–134.
[6] S.K. Aghda, D. Bogdanovski, L. Löfler, H.H. Sua, L. Patterer, D.M. Holzapfel, A. Le Febvrier, M. Hans, D. Primetzhofer, J.M. Schneider, Valence electron concentration-and N vacancy-induced elasticity in cubic early transition metal nitrides, Acta Mater. 255 (2023) 119078.
[7] D.G. Sangiovanni, L. Hultman, V. Chirita, Supertoughening in B1 transition metal nitride alloys by increased valence electron concentration, Acta Mater. 59 (5) (2011) 2121–2134.
[8] H. Kindlund, D.G. Sangiovanni, I. Petrov, J.E. Greene, L. Hultman, A review of the intrinsic ductility and toughness of hard transition-metal nitride alloy thin films, Thin. Solid. Films. 688 (2019) 137479.
[9] D.G. Sangiovanni, K. Kaufmann, K. Vecchio, Valence electron concentration as key parameter to control the fracture resistance of refractory high-entropy carbides, Sci. Adv. 9 (37) (2023) eadi2960.
[10] P.H. Mayrhofer, C. Mitterer, L. Hultman, H. Clemens, Microstructural design of hard coatings, Prog. Mater. Sci. 51 (8) (2006) 1032–1114.
[11] Z. Chen, Y. Huang, N. Koutná, Z. Gao, D.G. Sangiovanni, S. Fellner, G. Haberfehlner, S. Jin, P.H. Mayrhofer, G. Kothleitner, Z. Zhang, Large mechanical properties enhancement in ceramics through vacancy-mediated unit cell disturbance, Nat. Commun. 14 (1) (2023) 8387.
[12] Z. Wu, Y. Zhao, W. Jin, B. Jia, J. Wang, T. Ma, Recent progress of vacancy engineering for electrochemical energy conversion related applications, Adv. Funct. Mater. 31 (9) (2021) 2009070.
[13] J. Pflüger, J. Fink, W. Weber, K. Bohnen, G. Crecelius, Dielectric properties of TiC x, TiN x, VC x, and VN x from 1.5 to 40 eV determined by electron-energy-loss spectroscopy, Phys. Rev. B 30 (3) (1984) 1155.
[14] N. Schalk, J.T.S. Fotso, D. Holec, G. Jakopic, A. Fian, V.L. Terziyska, R. Daniel, C. Mitterer, Influence of varying nitrogen partial pressures on microstructure, mechanical and optical properties of sputtered TiAlON coatings, Acta Mater. 119 (2016) 26–34.
[15] S. Fabris, A.T. Paxton, M.W. Finnis, A stabilization mechanism of zirconia based on oxygen vacancies only, Acta Mater. 50 (20) (2002) 5171–5178.
[16] H. Euchner, P. Mayrhofer, H. Riedl, F. Klimashin, A. Limbeck, P. Polcik, S. Kolozsvari, Solid solution hardening of vacancy stabilized Ti x W 1− x B 2, Acta Mater. 101 (2015) 55–61.
[17] F.F. Klimashin, H. Euchner, P.H. Mayrhofer, Computational and experimental studies on structure and mechanical properties of Mo–Al–N, Acta Mater. 107 (2016) 273–278.
[18] F.F. Klimashin, J. Klusoň, M. Učík, R. Žemlička, M. Jílek, A. Lümkemann, J. Michler, T.E.J. Edwards, High-power-density sputtering of industrial-scale targets: case study of (Al,Cr)N, Mater. Des. 237 (2024) 112553.
[19] V. Kouznetsov, K. Macak, J.M. Schneider, U. Helmersson, I. Petrov, A novel pulsed magnetron sputter technique utilizing very high target power densities, Surf. Coat. Technol. 122 (2–3) (1999) 290–293.
[20] J. Gudmundsson, N. Brenning, D. Lundin, U. Helmersson, High power impulse magnetron sputtering discharge, J. Vacuum Sci. Technol. A 30 (3) (2012).
[21] J. Vetter, T. Shimizu, D. Kurapov, T. Sasaki, J. Mueller, D. Stangier, M. Esselbach, Industrial application potential of high power impulse magnetron sputtering for wear and corrosion protection coatings, J. Appl. Phys. 134 (16) (2023) 160701.
[22] J. Vetter, Coined by J. Vetter in private discussion, 2024.
[23] D. Rafaja, C. Wustefeld, C. Baehtz, V. Klemm, M. Dopita, M. Motylenko, C. Michotte, M. Kathrein, Effect of internal interfaces on hardness and thermal stability of nanocrystalline Ti0.5Al0.5N coatings, Metall. Mater. Trans. -Phys. Metall. Mater. Sci. 42a (3) (2011) 559–569.
[24] M. Döbeli, C. Kottler, M. Stocker, S. Weinmann, H.-A. Synal, M. Grajcar, M. Suter, Gas ionization chambers with silicon nitride windows for the detection and identification of low energy ions, Nucl. Instrum. Methods Phys. Res. Sect. B: Beam Interact. Mater. Atoms 219 (2004) 415–419.
[25] T. Chudoba, D. Schwenk, P. Reinstädt, M. Griepentrog, High-precision calibration of indenter area function and instrument compliance, JOM 74 (6) (2022) 2179–2194.
[26] F.F. Klimashin, P.H. Mayrhofer, Ab initio-guided development of super-hard Mo–Al–Cr–N coatings, Scr. Mater. 140 (2017) 27–30.
[27] W.C. Oliver, G.M. Pharr, An improved technique for determining hardness and elastic-modulus using load and displacement sensing indentation experiments, J. Mater. Res. 7 (6) (1992) 1564–1583.
[28] A.C. Fischer-Cripps, Critical review of analysis and interpretation of nanoindentation test data, Surf. Coat. Technol. 200 (14–15) (2006) 4153–4165.
[29] L. Zhou, D. Holec, P.H. Mayrhofer, First-principles study of elastic properties of cubic $Cr_{1-x}Al_xN$ alloys, J. Appl. Phys. 113 (4) (2013) 043511.
[30] M. Sebastiani, K. Johanns, E.G. Herbert, F. Carassiti, G.M. Pharr, A novel pillar indentation splitting test for measuring fracture toughness of thin ceramic coatings, Philos. Mag. 95 (16–18) (2015) 1928–1944.
[31] M. Ghidelli, M. Sebastiani, K.E. Johanns, G.M. Pharr, Effects of indenter angle on micro-scale fracture toughness measurement by pillar splitting, J. Am. Ceram. Soc. 100 (12) (2017) 5731–5738.
[32] K.-D. Bouzakis, S. Kombogiannis, A. Antoniadis, N. Vidakis, Gear hobbing cutting process simulation and tool wear prediction models, J. Manuf. Sci. Eng. 124 (1) (2002) 42–51.
[33] A. Lümkemann, M. Beutner, M. Morstein, M. Köchig, M.W.T. Cselle, B. Karpuschewski, A New Generation of PVD Coatings For High-Performance Gear Hobbing, Preprint from A Coatings Conference, Thessaloniki, Greece, 2014.
[34] D. Gehringer, M. Friák, D. Holec, Models of configurationally-complex alloys made simple, Comput. Phys. Commun. 286 (2023) 108664.
[35] G. Kresse, J. Furthmuller, Efficient iterative schemes for ab initio total-energy calculations using a plane-wave basis set, Phys. Rev. B Condens. Matter. 54 (16) (1996) 11169–11186.
[36] G. Kresse, J. Hafner, Ab initio molecular dynamics for liquid metals, Phys. Rev. B Condens. Matter. 47 (1) (1993) 558–561.
[37] J.P. Perdew, K. Burke, M. Ernzerhof, Generalized gradient approximation made simple, Phys. Rev. Lett. 77 (18) (1996) 3865–3868.
[38] A. Khein, D.J. Singh, C.J. Umrigar, All-electron study of gradient corrections to the local-density functional in metallic systems, Phys. Rev. B Condens. Matter. 51 (7) (1995) 4105–4109.
[39] P.H. Mayrhofer, D. Music, T. Reeswinkel, H.G. Fuß, J.M. Schneider, Structure, elastic properties and phase stability of Cr1–xAlxN, Acta Mater. 56 (11) (2008) 2469–2475.
[40] L. Wang, X. Han, P. Liu, Y. Yue, Z. Zhang, E. Ma, In situ observation of dislocation behavior in nanometer grains, Phys. Rev. Lett. 105 (13) (2010) 135501.
[41] J. Salamania, D. Sangiovanni, A. Kraych, K.C. Kwick, I. Schramm, L. Johnson, R. Boyd, B. Bakhit, T. Hsu, M. Mrovec, Elucidating dislocation core structures in titanium nitride through high-resolution imaging and atomistic simulations, Mater. Des. 224 (2022) 111327.
[42] X. Gu, Z. Zhang, M. Bartosik, P.H. Mayrhofer, H. Duan, Dislocation densities and alternating strain fields in CrN/AlN nanolayers, Thin. Solid. Films. 638 (2017) 189–200.
[43] J. Buchinger, A. Wagner, Z. Chen, Z. Zhang, D. Holec, P.H. Mayrhofer, M. Bartosik, Fracture toughness trends of modulus-matched TiN/(Cr, Al) N thin film superlattices, Acta Mater. 202 (2021) 376–386.
[44] A. Drnovšek, H.T. Vo, M.R. de Figueiredo, S. Kolozsvári, P. Hosemann, R. Franz, High temperature fracture toughness of single-layer CrAlN and CrAlSiN hard coatings, Surf. Coat. Technol. 409 (2021) 126909.
[45] B. Karpuschewski, M. Beutner, M. Köchig, C. Härtling, Influence of the tool profile on the wear behaviour in gear hobbing, CIRP. J. Manuf. Sci. Technol. 18 (2017) 128–134.
[46] D.B. Williams, C.B. Carter, The Transmission Electron Microscope, Springer, 1996.
[47] L. Hultman, J.E. Sundgren, J. Greene, Formation of polyhedral N2 bubbles during reactive sputter deposition of epitaxial TiN (100) films, J. Appl. Phys. 66 (2) (1989) 536–544.
[48] R.R. Manory, G. Kimmel, X-ray characterization of TiNx films with CaF2-type structure, Thin. Solid. Films. 150 (2–3) (1987) 277–282.
[49] D. Frost, C. McDowell, The dissociation energy of the nitrogen molecule, Proc. R. Soc. London. Ser. A. Math. Phys. Sci. 236 (1205) (1956) 278–284.
[50] Z. Wang, S.A. Cohen, D.N. Ruzic, M. Goeckner, Nitrogen atom energy distributions in a hollow-cathode planar sputtering magnetron, Phys. Rev. E 61 (2) (2000) 1904.
[51] K. Sarakinos, J. Alami, P. Karimi, D. Severin, M. Wuttig, The role of backscattered energetic atoms in film growth in reactive magnetron sputtering of chromium nitride, J. Phys. D. Appl. Phys. 40 (3) (2007) 778.
[52] G. Greczynski, L. Hultman, Time and energy resolved ion mass spectroscopy studies of the ion flux during high power pulsed magnetron sputtering of Cr in Ar and Ar/N2 atmospheres, Vacuum. 84 (9) (2010) 1159–1170.
[53] D. Depla, G. Buyle, J. Haemers, R. De Gryse, Discharge voltage measurements during magnetron sputtering, Surf. Coat. Technol. 200 (14–15) (2006) 4329–4338.
[54] J.-F. Tang, C.-Y. Lin, F.-C. Yang, C.-L. Chang, Influence of nitrogen content and bias voltage on residual stress and the tribological and mechanical properties of CrAlN films, Coatings 10 (6) (2020) 546.
[55] S. Schiller, G. Beister, W. Sieber, Reactive high rate DC sputtering: deposition rate, stoichiometry and features of TiOx and TiNx films with respect to the target mode, Thin. Solid. Films. 111 (3) (1984) 259–268.
[56] F. Adibi, I. Petrov, J. Greene, L. Hultman, J.E. Sundgren, Effects of high-flux low-energy (20–100 eV) ion irradiation during deposition on the microstructure and

preferred orientation of Ti0. 5Al0. 5N alloys grown by ultra-high-vacuum reactive magnetron sputtering, J. Appl. Phys. 73 (12) (1993) 8580–8589.
[57] I. Petrov, F. Adibi, J. Greene, L. Hultman, J.E. Sundgren, Average energy deposited per atom: a universal parameter for describing ion-assisted film growth? Appl. Phys. Lett. 63 (1) (1993) 36–38.
[58] F. Ferreira, J. Oliveira, A. Cavaleiro, CrN thin films deposited by HiPIMS in DOMS mode, Surf. Coat. Technol. 291 (2016) 365–375.
[59] I. Goldfarb, J. Pelleg, L. Zevin, N. Croitoru, Lattice distortion in thin films of IVB metal (Ti, Zr, Hr) nitrides, Thin. Solid. Films. 200 (1) (1991) 117–127.
[60] V. Valvoda, A. Perry, L. Hultman, J. Musil, S. Kadlec, On picostructural models of physically vapor-deposited films of titanium nitride, Surf. Coat. Technol. 49 (1–3) (1991) 181–187.
[61] E. Mozafari, B. Alling, P. Steneteg, I.A. Abrikosov, Role of N defects in paramagnetic CrN at finite temperatures from first principles, Phys. Rev. B 91 (9) (2015) 094101.
[62] J. Hnilica, P. Klein, M. Ucík, S. Debnárová, J. Kluson, P. Vasina, On direct-current magnetron sputtering at industrial conditions with high ionization fraction of sputtered species, Surf. Coat. Technol. 487 (2024) 131028.
[63] I. Petrov, P.B. Barna, L. Hultman, J.E. Greene, Microstructural evolution during film growth, J. Vacuum Sci. Technol. A 21 (5) (2003) S117–S128.
[64] A. Anders, Tutorial: reactive high power impulse magnetron sputtering (R-HiPIMS), J. Appl. Phys. 121 (17) (2017) 171101.
[65] J. Pelleg, L.Z. Zevin, S. Lungo, N. Croitoru, Reactive-sputter-deposited tin films on glass substrates, Thin. Solid. Films. 197 (1–2) (1991) 117–128.
[66] U. Oh, J.H. Je, Effects of strain energy on the preferred orientation of TiN thin films, J. Appl. Phys. 74 (3) (1993) 1692–1696.
[67] C. Tholander, B. Alling, F. Tasnádi, J.E. Greene, L. Hultman, Effect of Al substitution on Ti, Al, and N adatom dynamics on TiN (001),(011), and (111) surfaces, Surf. Sci. 630 (2014) 28–40.
[68] V. Antonov, I. Iordanova, Density-functional study of the crystallographic structure of chromium nitride films. Journal of Physics: Conference Series, IOP Publishing, 2010 012043.
[69] J.O. Kim, J.D. Achenbach, P.B. Mirkarimi, S.A. Barnett, Acoustic-microscopy measurements of the elastic properties of TiN/(V x Nb 1−N superlattices, Phys. Rev. B 48 (3) (1993) 1726.
[70] D. Gall, S. Kodambaka, M.A. Wall, I. Petrov, J.E. Greene, Pathways of atomistic processes on TiN(001) and (111) surfaces during film growth: an ab initio study, J. Appl. Phys. 93 (11) (2003) 9086–9094.
[71] B. Alling, P. Steneteg, C. Tholander, F. Tasnádi, I. Petrov, J.E. Greene, L. Hultman, Configurational disorder effects on adatom mobilities on Ti 1− x Al x N (001) surfaces from first principles, Phys. Rev. B 85 (24) (2012) 245422.
[72] J.E. Greene, J.E. Sundgren, L. Hultman, I. Petrov, D.B. Bergstrom, Development of preferred orientation in polycrystalline tin layers grown by ultrahigh-vacuum reactive magnetron sputtering, Appl. Phys. Lett. 67 (20) (1995) 2928–2930.
[73] C.-S. Shin, D. Gall, Y.-W. Kim, N. Hellgren, I. Petrov, J. Greene, Development of preferred orientation in polycrystalline NaCl-structure δ-TaN layers grown by reactive magnetron sputtering: role of low-energy ion surface interactions, J. Appl. Phys. 92 (9) (2002) 5084–5093.
[74] Y. Andoh, K. Ogata, H. Yamaki, S. Sakai, Crystalline orientation control by the IVD method, Nucl. Instrum. Methods Phys. Res. Section B: Beam Interact. Mater. Atoms 39 (1–4) (1989) 158–161.
[75] A. Hörling, L. Hultman, M. Odén, J. Sjölén, L. Karlsson, Mechanical properties and machining performance of Ti1− xAlxN-coated cutting tools, Surf. Coat. Technol. 191 (2–3) (2005) 384–392.
[76] J. Lin, J.J. Moore, B. Mishra, M. Pinkas, W.D. Sproul, J. Rees, Effect of asynchronous pulsing parameters on the structure and properties of CrAlN films deposited by pulsed closed field unbalanced magnetron sputtering (P-CFUBMS), Surf. Coat. Technol. 202 (8) (2008) 1418–1436.
[77] R. Hollerweger, L. Zhou, D. Holec, C. Koller, R. Rachbauer, P. Polcik, P. H. Mayrhofer, Controlling microstructure, preferred orientation, and mechanical properties of Cr-Al-N by bombardment and alloying with Ta, J. Appl. Phys. 119 (6) (2016) 065304.
[78] K. Bobzin, T. Brögelmann, N. Kruppe, M. Engels, A. Von Keudell, A. Hecimovic, A. Ludwig, D. Grochla, L. Banko, Fundamental study of an industrial reactive HPPMS (Cr, Al) N process, J. Appl. Phys. 122 (1) (2017) 015302.
[79] L. Banko, S. Ries, D. Grochla, M. Arghavani, S. Salomon, J. Pfetzing-Micklich, A. Kostka, D. Rogalla, J. Schulze, P. Awakowicz, Effects of the ion to growth flux ratio on the constitution and mechanical properties of Cr1–x-Al x-N thin films, ACS. Comb. Sci. 21 (12) (2019) 782–793.
[80] Y. Liu, J.C. Ding, B.R. Zhang, J.J. Chen, C.R. Tang, R.Y. Zhu, J. Zheng, Effect of duty cycle on microstructure and mechanical properties of AlCrN coatings deposited by HiPIMS, Vacuum. 205 (2022) 111409.
[81] S. Kadlec, J. Musil, V. Valvoda, W.-D. Münz, H. Petersein, J. Schroeder, TiN films grown by reactive magnetron sputtering with enhanced ionization at low discharge pressures, Vacuum. 41 (7–9) (1990) 2233–2238.
[82] N.H. Hoang, D. McKenzie, W. McFall, Y. Yin, Properties of TiN films deposited at low temperature in a new plasma-based deposition system, J. Appl. Phys. 80 (11) (1996) 6279–6285.
[83] J. Zhao, X. Wang, Z.Y. Chen, S. Yang, T. Shi, X. Liu, Overall energy model for preferred growth of TiN films during filtered arc deposition, J. Phys. D. Appl. Phys. 30 (1) (1997) 5.
[84] T. Hurkmans, D. Lewis, H. Paritong, J. Brooks, W. Münz, Influence of ion bombardment on structure and properties of unbalanced magnetron grown CrNx coatings, Surf. Coat. Technol. 114 (1) (1999) 52–59.
[85] S. Grasser, R. Daniel, C. Mitterer, Microstructure modifications of CrN coatings by pulsed bias sputtering, Surf. Coat. Technol. 206 (22) (2012) 4666–4671.
[86] S. Han, J. Lin, X. Guo, S. Tsai, Y. Su, J. Huang, F.-H. Lu, H. Shih, The effect of Cr interlayer on the microstructure of CrN coatings on steel, Thin. Solid. Films. 377 (2000) 578–584.
[87] C. Gautier, H. Moussaoui, F. Elstner, J. Machet, Comparative study of mechanical and structural properties of CrN films deposited by dc magnetron sputtering and vacuum arc evaporation, Surf. Coat. Technol. (86–87) (1996) 254–262.
[88] A. Ehiasarian, W.-D. Münz, L. Hultman, U. Helmersson, I. Petrov, High power pulsed magnetron sputtered CrNx films, Surf. Coat. Technol. 163 (2003) 267–272.
[89] Q. Luo, S. Yang, K. Cooke, Hybrid HIPIMS and DC magnetron sputtering deposition of TiN coatings: deposition rate, structure and tribological properties, Surf. Coat. Technol. 236 (2013) 13–21.
[90] G. Farges, E. Beauprez, M. Sainte Catherine, Crystallographic structure of sputtered cubic δ-VNx films: influence of basic deposition parameters, Surf. Coat. Technol. 61 (1–3) (1993) 238–244.
[91] S. Nayak, T.-W. Hsu, R. Boyd, J. Gibmeier, N. Schell, J. Birch, L. Rogström, M. Odén, Dynamic evolution of internal stress, grain growth, and crystallographic texture in arc-evaporated AlTiN thin films using in-situ synchrotron x-ray diffraction, Acta Mater. 272 (2024) 119899.
[92] A. Perry, On the existence of point defects in physical vapor deposited films of TiN, ZrN, and HfN, J. Vacuum Sci. Technol. A: Vacuum, Surf. Films 6 (3) (1988) 2140–2148.
[93] A. Perry, V. Valvoda, D. Rafaja, On the residual stress and picostructure of titanium nitride films—II. A picostructural model, Vacuum. 45 (1) (1994) 11–14.
[94] L. Hultman, J. Sundgren, Structure/property relationships for hard coatings, in: R. Bunshah (Ed.), Handbook of Hard Coatings: Deposition Technologies, Properties and Applications, 2001, pp. 108–180.
[95] P.H. Mayrhofer, H. Clemens, F.D. Fischer, Materials science-based guidelines to develop robust hard thin film materials, Prog. Mater. Sci. (2024) 101323.
[96] C.M. Lauener, L. Petho, M. Chen, Y. Xiao, J. Michler, J.M. Wheeler, Fracture of silicon: influence of rate, positioning accuracy, FIB machining, and elevated temperatures on toughness measured by pillar indentation splitting, Mater. Des. 142 (2018) 340–349.
[97] J.P. Best, J. Zechner, J.M. Wheeler, R. Schoeppner, M. Morstein, J. Michler, Small-scale fracture toughness of ceramic thin films: the effects of specimen geometry, ion beam notching and high temperature on chromium nitride toughness evaluation, Philos. Mag. 96 (32–34) (2016) 3552–3569.
[98] M. Bartosik, C. Rumeau, R. Hahn, Z.L. Zhang, P.H. Mayrhofer, Fracture toughness and structural evolution in the TiAlN system upon annealing, Sci. Rep.-U.K. 7 (1) (2017) 16476.
[99] G.T. Hahn, The influence of microstructure on brittle-fracture toughness, Metall. Trans. A 15 (6) (1984) 947–959.
[100] S.M. Wiederhorn, Brittle-fracture and toughening mechanisms in ceramics, Annu. Rev. Mater. Sci. 14 (1) (1984) 373–403.
[101] S. Liu, J.M. Wheeler, C. Davis, W. Clegg, X. Zeng, The effect of Si content on the fracture toughness of CrAlN/Si3N4 coatings, J. Appl. Phys. 119 (2) (2016) 025305.
[102] L. Porz, A.J. Klomp, X. Fang, N. Li, C. Yildirim, C. Detlefs, E. Bruder, M. Höfling, W. Rheinheimer, E.A. Patterson, Dislocation-toughened ceramics, Mater. Horiz. 8 (5) (2021) 1528–1537.
[103] A.G. Evans, Perspective on the development of high-toughness ceramics, J. Am. Ceram. Soc. 73 (2) (1990) 187–206.
[104] R.O. Ritchie, The conflicts between strength and toughness, Nat. Mater. 10 (11) (2011) 817–822.
[105] L. Liu, Q. Yu, Z. Wang, J. Ell, M.X. Huang, R.O. Ritchie, Making ultrastrong steel tough by grain-boundary delamination, Science (1979) 368 (6497) (2020) 1347–1352.
[106] M. Gell, E. Smith, The propagation of cracks through grain boundaries in polycrystalline 3% silicon-iron, Acta Metall. 15 (2) (1967) 253–258.
[107] T. Watanabe, S. Tsurekawa, Toughening of brittle materials by grain boundary engineering, Mater. Sci. Eng. A-Struct. 387 (2004) 447–455.
[108] R. Daniel, M. Meindlhumer, W. Baumegger, J. Zalesak, B. Sartory, M. Burghammer, C. Mitterer, J. Keckes, Grain boundary design of thin films: using tilted brittle interfaces for multiple crack deflection toughening, Acta Mater. 122 (2017) 130–137.
[109] R. Daniel, M. Meindlhumer, W. Baumegger, J. Todt, J. Zalesak, T. Ziegelwanger, C. Mitterer, J. Keckes, Anisotropy of fracture toughness in nanostructured ceramics controlled by grain boundary design, Mater. Des. 161 (2019) 80–85.
[110] M. Schlogl, C. Kirchlechner, J. Paulitsch, J. Keckes, P.H. Mayrhofer, Effects of structure and interfaces on fracture toughness of CrN/AlN multilayer coatings, Scr. Mater. 68 (12) (2013) 917–920.
[111] R. Hahn, M. Bartosik, R. Soler, C. Kirchlechner, G. Dehm, P.H. Mayrhofer, Superlattice effect for enhanced fracture toughness of hard coatings, Scr. Mater. 124 (2016) 67–70.
[112] R. Hahn, A.A. Tymoszuk, T. Wojcik, E. Ntemou, O. Hunold, P. Polcik, S. Kolozsvari, D. Primetzhofer, P.H. Mayrhofer, H. Riedl, Unraveling the superlattice effect for hexagonal transition metal diboride coatings, Scr. Mater. 235 (2023) 115599.
[113] R. Daniel, M. Meindlhumer, J. Zalesak, W. Baumegger, J. Todt, T. Ziegelwanger, J.F. Keckes, C. Mitterer, J. Keckes, Multi-scale interface design of strong and damage resistant hierarchical nanostructured materials, Mater. Des. 196 (2020) 109169.
[114] S. Kumar, D. Wolfe, M. Haque, Dislocation shielding and flaw tolerance in titanium nitride, Int. J. Plast. 27 (5) (2011) 739–747.
[115] Y. Huang, Z. Chen, M. Meindlhumer, R. Hahn, D. Holec, T. Leiner, V. Maier-Kiener, Y. Zheng, Z. Zhang, L. Hatzenbichler, Harvesting superior intrinsic

plasticity in nitride ceramics with negative stacking fault energy, Acta Mater. (2025) 120774.
[116] B. Warcholinski, A. Gilewicz, P. Myslinski, E. Dobruchowska, D. Murzynski, Structure and properties of AlCrN coatings deposited using cathodic arc evaporation, Coatings 10 (8) (2020) 793.
[117] M. Moreno, J.M. Andersson, R. Boyd, M.P. Johansson-Jöesaar, L.J. Johnson, M. Odén, L. Rogström, Crater wear mechanism of TiAlN coatings during high-speed metal turning, Wear. 484 (2021) 204016.
[118] H.E. Rebenne, D.G. Bhat, Review of CVD TiN coatings for wear-resistant applications: deposition processes, properties and performance, Surf. Coat. Technol. 63 (1–2) (1994) 1–13.
[119] F. Svahn, Å. Kassman-Rudolphi, E. Wallén, The influence of surface roughness on friction and wear of machine element coatings, Wear. 254 (11) (2003) 1092–1098.
[120] M. Tkadletz, C. Mitterer, B. Sartory, I. Letofsky-Papst, C. Czettl, C. Michotte, The effect of droplets in arc evaporated TiAlTaN hard coatings on the wear behavior, Surf. Coat. Technol. 257 (2014) 95–101.
[121] S.S. Kim, J.G. Han, S.Y. Lee, Deposition behaviours of CrN films on the edge area by cathodic arc plasma deposition process, Thin. Solid. Films. 334 (1–2) (1998) 133–139.
[122] M. Meindlhumer, N. Jäger, S. Spor, M. Rosenthal, J. Keckes, H. Hruby, C. Mitterer, R. Daniel, J. Keckes, J. Todt, Nanoscale residual stress and microstructure gradients across the cutting edge area of a TiN coating on WCCo, Scr. Mater. 182 (2020) 11–15.
[123] P. Hedenqvist, M. Olsson, S. Söderberg, Influence of TiN coating on wear of high speed steel tools as studied by new laboratory wear test, Surf. Eng. 5 (2) (1989) 141–150.
[124] J. Gerth, M. Larsson, U. Wiklund, F. Riddar, S. Hogmark, On the wear of PVD-coated HSS hobs in dry gear cutting, Wear. 266 (3–4) (2009) 444–452.
[125] A. Leyland, A. Matthews, On the significance of the H/E ratio in wear control: a nanocomposite coating approach to optimised tribological behaviour, Wear. 246 (1–2) (2000) 1–11.
[126] T. Tsui, G. Pharr, W. Oliver, C. Bhatia, R. White, S. Anders, A. Anders, I. Brown, Nanoindentation and nanoscratching of hard carbon coatings for magnetic disks, MRS Proc. (1995) 447.
[127] X.Z. Ding, X.T. Zeng, Y.C. Liu, Structure and properties of CrAlSiN nanocomposite coatings deposited by lateral rotating cathod arc, Thin. Solid. Films. 519 (6) (2011) 1894–1900.
[128] X. Chen, Y. Du, Y.-W. Chung, Commentary on using H/E and H3/E2 as proxies for fracture toughness of hard coatings, Thin. Solid. Films. 688 (2019) 137265.
[129] B.D. Beake, The influence of the H/E ratio on wear resistance of coating systems–insights from small-scale testing, Surf. Coat. Technol. 442 (2022) 128272.